REPORT DOCUMENTATION PAGE

AFRL-SR-AR-TR-05-

0502

1. AGENCY USE ONLY *(Leave blank)*	2. REPORT DATE	3. REPORT
		Final

4. TITLE AND SUBTITLE
Time Exposure Acoustics for Imaging Underground Structures

5. FUNDING NUMBERS
F49620-03-C-0111

6. AUTHOR(S)
Dr. Won

7. PERFORMING ORGANIZATION NAME(S) AND ADDRESS(ES)
Geophex, LTD

8. PERFORMING ORGANIZATION REPORT NUMBER

9. SPONSORING/MONITORING AGENCY NAME(S) AND ADDRESS(ES)
AFOSR

NM

10. SPONSORING/MONITORING AGENCY REPORT NUMBER

11. SUPPLEMENTARY NOTES

12a. DISTRIBUTION AVAILABILITY STATEMENT

Approved for public release,
distribution unlimited

12b. DISTRIBUTION CODE

13. ABSTRACT *(Maximum 200 words)*

The coalmine study demonstrates that passive imaging is feasible under realistic conditions, but improvements are certainly possible. For example, some noticeable phase rotation of the seismic traces across the array is evident when the traces are plotted (e.g., as in Figure 11 but at higher magnification). The phase rotation is probably due in part to dispersion of the seismic waves as a function of path length (greater path lengths imply greater dispersion). Phase rotation will degrade the resolution of the image. Simulations show that images derived from idealized data in the absence of phase rotation are of higher quality. No phase rotation implies that the signals recorded at different geophones are merely delayed versions of one another, where the delay is proportional to path length differences from the source to the receivers. Phase rotation due to dispersion can be corrected to some extend by inverse filtering, but was not attempted here. The reason for this is that rotation due to pure dispersion due only to path length differences was not clearly evident in the raw data, since systematic phase distortion as a function of path length was not seen across the array. This seems to imply that the phase distortion is probably due primarily to velocity inhomogeneities along the different propagation paths. Partial compensation for this might be achieved by incorporating a layered-earth model into the imaging algorithms, although this would require some a priori knowledge of the ~local stratigraphy.

14. SUBJECT TERMS			15. NUMBER OF PAGES
			16. PRICE CODE
17. SECURITY CLASSIFICATION OF REPORT	18. SECURITY CLASSIFICATION OF THIS PAGE	19. SECURITY CLASSIFICATION OF ABSTRACT	20. LIMITATION OF ABSTRACT

Time Exposure Acoustics for Imaging Underground Structures

Final Report to AFRL/AFOSR
September 30, 2005
Phase II STTR Contract F49620-03-C-0111
Geophex, Ltd., 605 Mercury Street, Raleigh, NC 27603

1. Introduction

The objective of this project was to investigate the feasibility of imaging subsurface acoustic sources generated artificially within an underground facility. One application identified as important by the Air Force is source location within a buried facility based on the passive monitoring of acoustic emissions from both stationary and moving equipment within such a facility. Another potential objective is to identify the type of source on the basis of its noise spectrum, although source characterization was beyond the scope of this project; rather, our goal was to examine and demonstrate the possibility of source imaging. The imaging techniques studied are, in principle, capable of reconstructing an intensity map, or image, of an extended source distribution using signals passively recorded by a geophone array deployed above ground.

Several approaches to passive seismic imaging have been studied in recent years. A method investigated by Shuster et al. [1] and Wapenaar et al. [2-5] termed "seismic interferometry," exploits the interference of a direct arrival with a scattered or secondary arrival, which may, for example, originate from backscattering from the surface. This approach is an elaboration of an idea by Claerbout [6] relating transmission and reflection seismograms using autocorrelated data in which one component originates from a free surface reflection. If the subsurface source is impulsive or very broadband, then the cross-correlation between the direct and secondary arrivals can bear a strong resemblance to a reflection seismogram.

An essential ingredient in the above methods is the interference between a direct and one or more secondary arrivals. The passive imaging methods investigated in the current project, however, differ in that they employ only the direct arrivals; no interference with a "reference wave" is required. In particular, two imaging algorithms of this kind have been previously published [7,8] by the PI and one outcome of this work was a clearer understanding of the relationship between these two techniques [9]. The earliest of these algorithms was derived for imaging acoustic emission sources in materials [7], while the second algorithm was intended for seismic imaging [8]. It is important to note that these algorithms do not use time delays across an array to "triangulate" on the source, which is inherently a nonlinear procedure. Rather, the algorithms are truly imaging methods, capable of mapping a spatially extended source. The imaging algorithms are linear in the intensity, and thus the source need not be spatially localized. In order for the algorithms to be linear, the assumption of a spatially incoherent source is required, meaning that the signals emitted from spatially distinct points within an extended source are assumed to be statistically uncorrelated.

In one imaging algorithm [7], termed "time-exposure acoustics," passive data acquired by an array of geophones are used to reconstruct a source image by backpropagating the signals into image space. This procedure bears some resemblance to time-domain migration. But, in contrast to the active source problem in which signals are transmitted into the ground, in the passive problem no time origin exists with respect to which the propagation delays can be referenced. That is, the signals are assumed emitted from the source in a continuous and random fashion. An essential idea described in [7] is to average with respect to this time origin. In particular, multiple images are reconstructed each with a different assumed time origin (the time at which the signal is emitted) and then these images are averaged on an intensity basis. This approach exploits the fact that the signal, either emitted from or scattered by a point in the subsurface, will create a wavefront that will manifest itself as a correlated signal across a receiving aperture on the surface. By coherently summing this signal and backpropagating to multiple source locations, one can develop an image of source intensity. As discussed in [7] image resolution is determined essentially by two factors: the source bandwidth and the array size.

The above method has been referred to as time-exposure acoustics (TEA) since the source is continuous and ever present, and, as a result, an image can be built up over time as data are continually accumulated. The underlying idea is to exploit the spatial coherence of signals which are correlated across an array to construct an image. When properly averaged, random fluctuations in an ensemble of images will diminish over time as new data are incorporated.

In the second source reconstruction algorithm [8] the source imaging problem is formulated as a tomographic reconstruction problem. Here, signals recorded by different pairs of geophones are cross correlated. The resultant correlation peak consists of an integration of the source intensity lying along a hyperbolic path (in a 2-D problem) or on the surface of a hyperboloid (in a 3-D problem) in which the coordinates of the two geophones define the foci of the hyperbola or hyperboloid. In this formulation, the correlation peaks may be regarded as the line integral of source intensity over this hyperbolic path (in 2-D) or as the surface integral of source intensity over a hyperboloid (in 3-D). It is shown in [9] that this method can be manipulated into a form that closely resembles the TEA algorithm, although this relationship may not be immediately obvious.

In the derivation of both algorithms, we assumed a scalar wave (acoustic) problem and a constant velocity; also mode conversion effects at the Earth's surface were neglected. These assumptions are made for simplicity, but the essential ideas presented here can be generalized in principle to more complex (and realistic) earth models.

In this final report, a review of the fundamental imaging equations of both algorithms is given in the Appendix. A detailed derivation of these equations and how the two algorithms are related can be found in [9]. The latter article was one outcome of this research. We shall also review below some key images derived from field data. We finally present new results obtained from data recorded over a coalmine during mining

operations. These last results demonstrate that actual images can be derived under realistic conditions. We conclude with suggestions for new areas of investigation that may further improve image quality.

2. Images of Points Sources -- Experimental Setup

Below, we compare the two reconstruction algorithms by applying them to the same field data. The data in these tests were acquired with a geophone array that recorded surface waves generated by a hammer source at a single location. Since the source and array are on the surface, the images are derived from surface (Rayleigh) waves only. These waves are dispersive and thus not in principle optimal for imaging since the algorithms are not designed to account for wave dispersion. Subsurface body waves in 3-D are not dispersive and should, in theory, provide better images. Nevertheless, as shown below, quite good images of the point sources were obtained using surface waves.

As a first test, seismic data were recorded by a seismograph attached to an 8 geophone array with a 15 foot spacing between elements. The seismograph was not triggered, but merely turned on for 30 seconds at a time; a large number of these 30 second intervals were recorded. The source was a hammer blow on a metal plate, which created surface waves that impinged upon the array. The source location was 45 feet from the array. A program was written to convert the SEG-2 file format generated by the seismograph into a binary file capable of being read by a MatLab program, which performed the image reconstructions.

Figure 1 shows the raw seismic data generated by the hammer source recorded by the 8 element array. The power spectrum of the signal recorded by one geophone is shown in Figure 2, which indicates a receiver bandwidth of about 5 Hz to 50 Hz. The surface sound velocity was estimated from the curvature of the impinging wavefront and knowledge of the source location to be approximately 600 ft/sec. In practice, when the source location is unknown, the velocity cannot be measured directly. A simple approach to estimating the correct velocity is to reconstruct multiple images using a range of velocities and then to select the velocity that provides the sharpest image. Various measures of image sharpness can be used for this purpose, e.g., borrowed from the field of adaptive optics. Sharpness criteria, for example, can be based on the mean entropy of the image or the mean spatial-frequency bandwidth of the image.

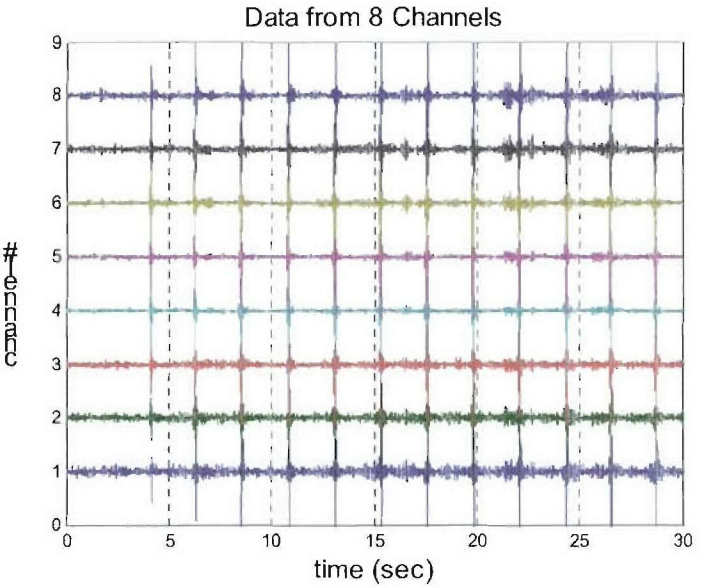

Figure 1. Data acquired over a 30 second time window with 8 geophones. Over this period of time, the ground was struck with a hammer 12 times. No seismograph triggering was used in acquiring the data. The sampling interval is 4 msec.

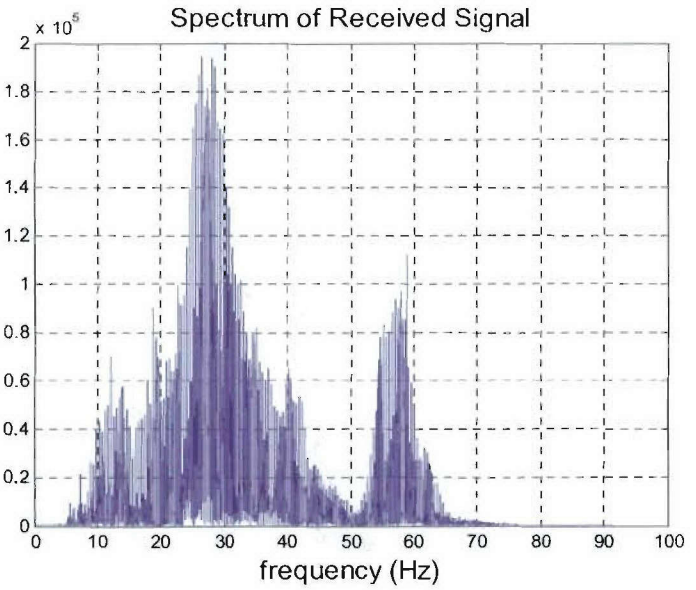

Figure 2. The power spectrum of a 30 second time record recorded by one geophone. This shows that the bandwidth is roughly 5 Hz to 50 Hz.

3. Reconstructed Images from Field Data

Both the time-domain migration and the cross-correlation algorithms were applied to two data sets (set 1 and set 2) recorded by the array. Figures 3 is a reconstructed image of the hammer source using the time-domain migration algorithm using data set 1. Figure 4 is the image of the source using the same data set, but employing the cross-correlation algorithm. In these reconstructions, 30 seconds of data were used. The cross-correlation images are similar to the time-domain migration images with the latter (Fig. 3) appearing to have somewhat better definition.

Figures 5 and 6 are images using data set 2 with the same two algorithms, respectively. This data set had somewhat superior signal to noise, and as a result the quality of the images appears somewhat better than those derived from data set 1.

Note that, in all of these images, the longitudinal resolution (resolution in the direction perpendicular to the array) is elongated compared to the lateral resolution. This is expected, since longitudinal resolution is determined solely by our ability to measure the curvature of the impinging wavefront. Lateral resolution, on the other hand, is primarily determined by the bandwidth of the noise and the array length. Resolution can be improved if one uses two linear arrays perpendicular to each other. This was done in a second experiment in which two arrays, each with seven elements, were arranged in the shape of an "L." The geophones were again spaced at 15 foot intervals. The image of a hammer source 45 ft. away from both arrays is shown in Figure 7 in which the time-domain migration algorithm was used. Using the same data, the image reconstructed using the cross-correlation algorithm is shown in Figure 8. With the L-shaped array, note that the resolution is tighter and more symmetrical compared to the images of Figure 3 through 6. Figure 9 show images using the time-domain migration algorithm with data from only a single leg of the array. In Figure 9, the array is in the y-direction and the image is elongated in the direction perpendicular to the array as expected. Figure 10 shows images using the time-domain migration algorithm with data from the other leg of the array (oriented in the x-direction). Again, elongation occurs perpendicular to the array. When the data from both legs are combined, we obtain the symmetrical image shown in Figure 7.

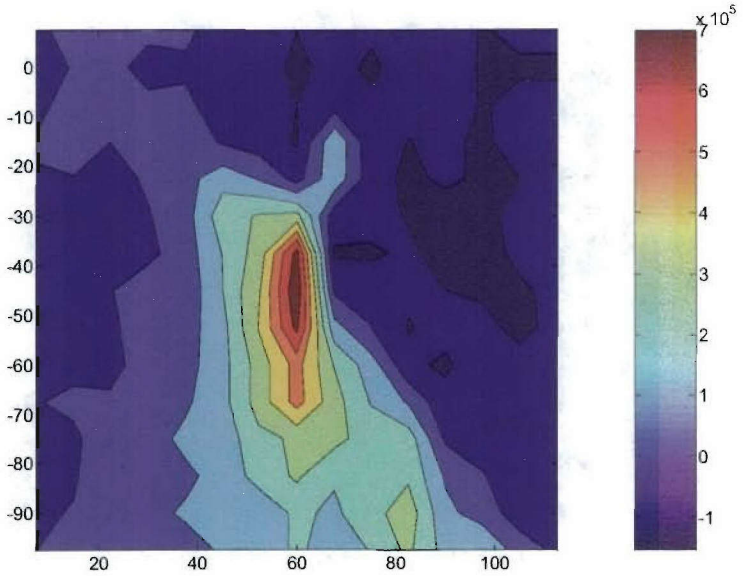

Figure 3. Image obtained using the time-domain migration algorithm (data set 1).

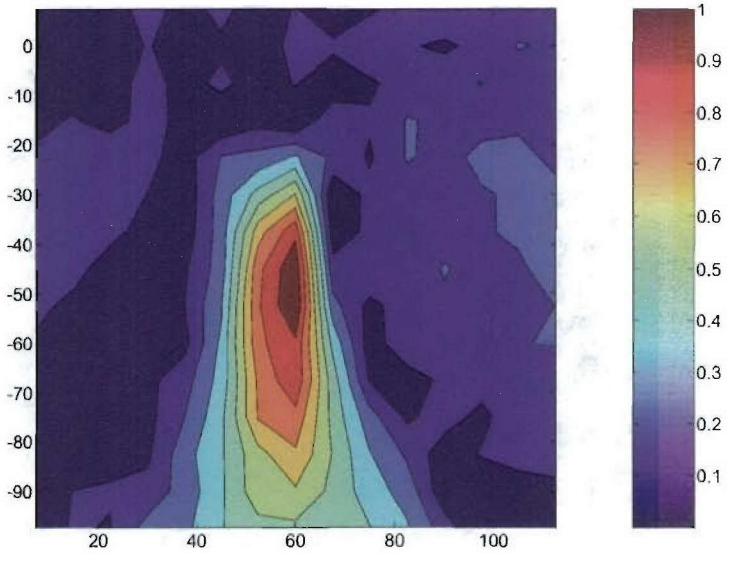

Figure 4. Contour image obtained using the cross-correlation algorithm (data set 1).

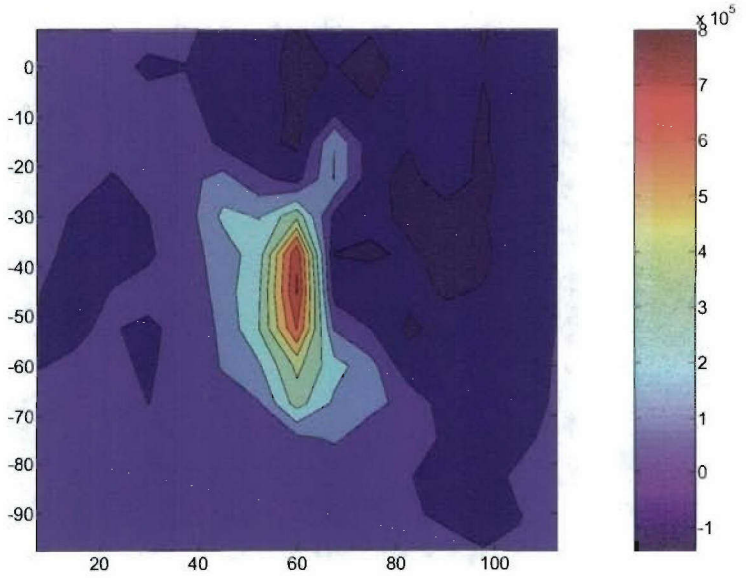

Figure 5. Image obtained using the time-domain migration algorithm (data set 2).

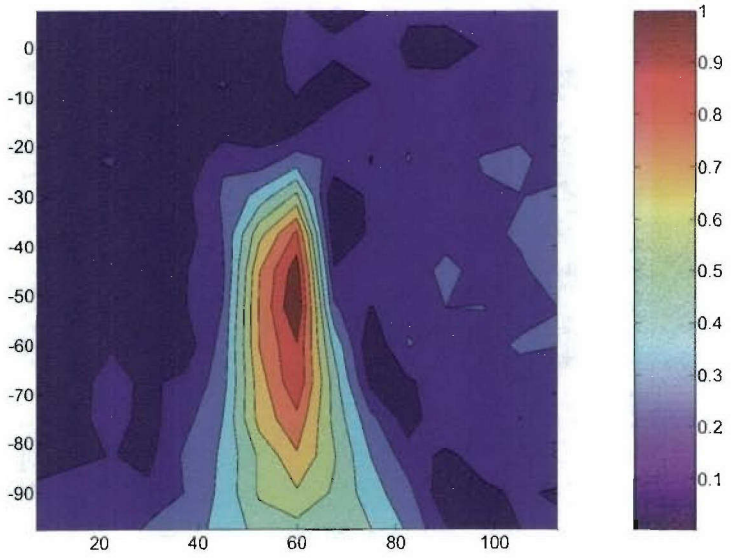

Figure 6. Image obtained using the cross-correlation algorithm (data set 2).

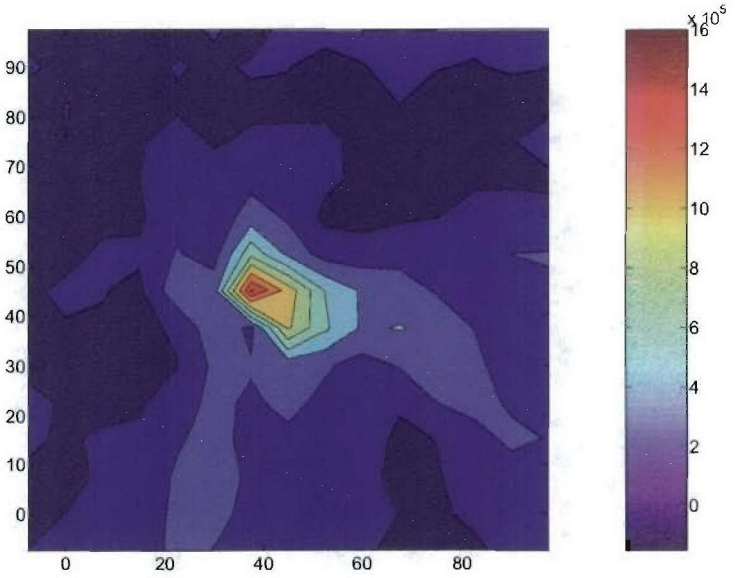

Figure 7. Image obtained from the L-shaped array data using the time-domain migration algorithm.

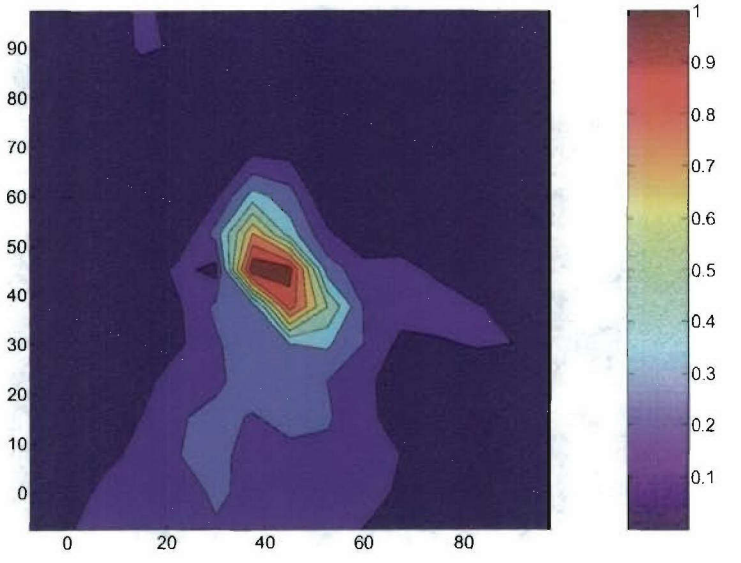

Figure 8. Image obtained from the L-shaped array data using the cross-correlation algorithm.

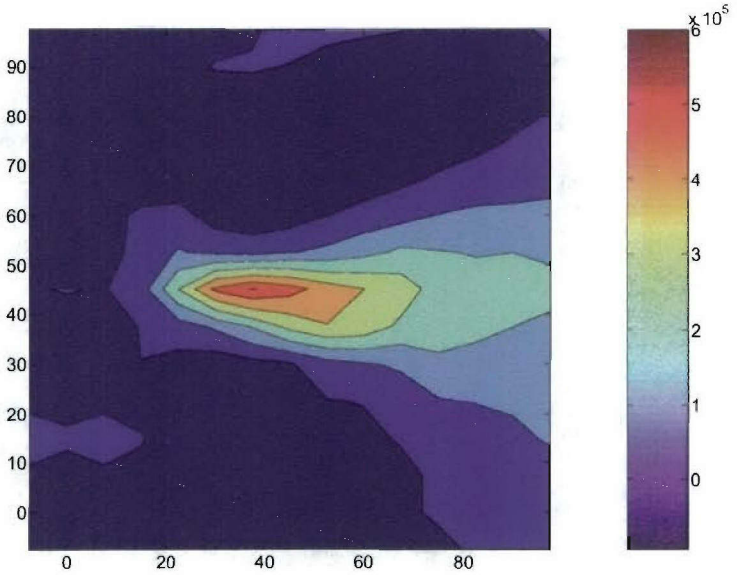

Figure 9. Image obtained from the first leg (7 geophones in the y direction) of the L-shaped array using the time-domain migration algorithm.

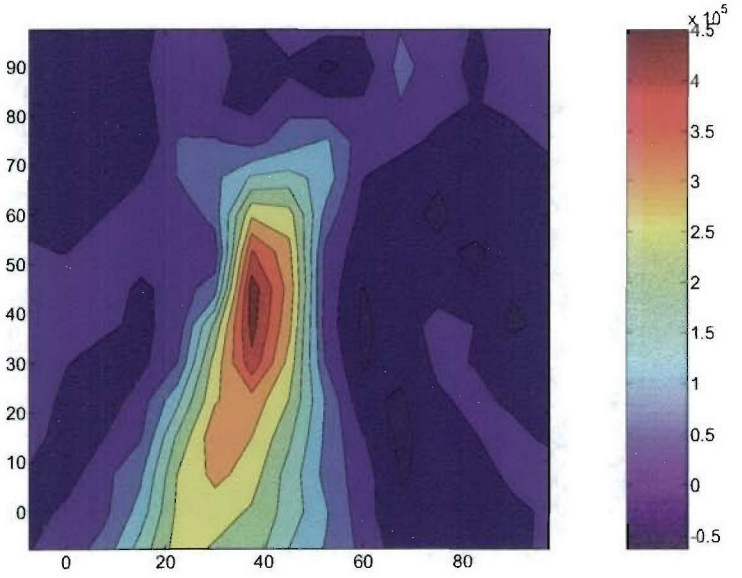

Figure 10. Image obtained from the second leg (7 geophones in the x direction) of the L-shaped array using the time-domain migration algorithm.

4. Coalmine Images

Two orientations of a linear array of geophones were used to record seismic data generated by mining operations over a coalmine in Salineville, Ohio on July 28, 2005. The arrays were laid out perpendicular to each other and an attempt was made to center the arrays directly over the region of the mine undergoing the cutting operation. The active mining face (the source region) was 350 ft below the surface. The array length was 420 ft with 29 geophones spaced at 15 ft intervals. Data were recorded with the first array (Line 1) over a period of about 40 minutes. For Line1, 40 30-second data records were recorded. The second array orientation (Line 2) was perpendicular to Line 1 with the same length and number of geophones. Line 2 recorded 38 30-second data records. Line 1 was oriented parallel to the mine tunnel, while Line 2 was oriented perpendicular to the mine tunnel. A sampling interval of 2 ms was used. Figure 11 shows the traces recorded by the 29 geophones from one 30 second data record. Notice the rather sudden onset of activity toward the end of this record. Figure 12 is the spectrum of a single trace, indicating some energy extending beyond 100 Hz, although most of the signal energy is confined to below 50 Hz.

Both imaging algorithms yielded very similar results, so we show below images obtained using the time-domain migration algorithm only. Figures 13a and 13b show 40 images reconstructed using the Line 1 data. Figure 13c shows the image obtained by combining all 40 records of data. Similarly, Figures 14a and 14b show 38 images reconstructed using Line 2. Figure 14c shows the image obtained by combining all 38 records of the Line 2 data. Some variability in the images shown in Figures 13a, 13b, 14a and 14b was to be expected since the operation of the mining machinery was intermittent over the 40 minute recording interval.

Using the Line 1 data set, it was found that a sound velocity of 9000 ft/sec placed the source image at the correct depth (350 ft). This is within the range of measured sound speeds for coal, estimated to be from about 6000 to 11,000 ft/sec [10]. However, for the Line 2 data set, a higher velocity of 12,000 ft/sec was required to place the source at the correct depth. This difference in apparent velocity may be due to several factors. One possibility is the presence of higher velocity material (e.g., sandstone) overlying the coal deposits. Another may be due to the fact that the Line 1 data were recorded with the array parallel to the mine tunnel, which could have artificially reduced the apparent velocity due to interaction with the tunnel (e.g., the tunnel acting as a wave guide creating multi-path effects). Future calibration tests using a known source (e.g., a hammer blow) at a known location within the mine could help explain the reasons for this velocity difference.

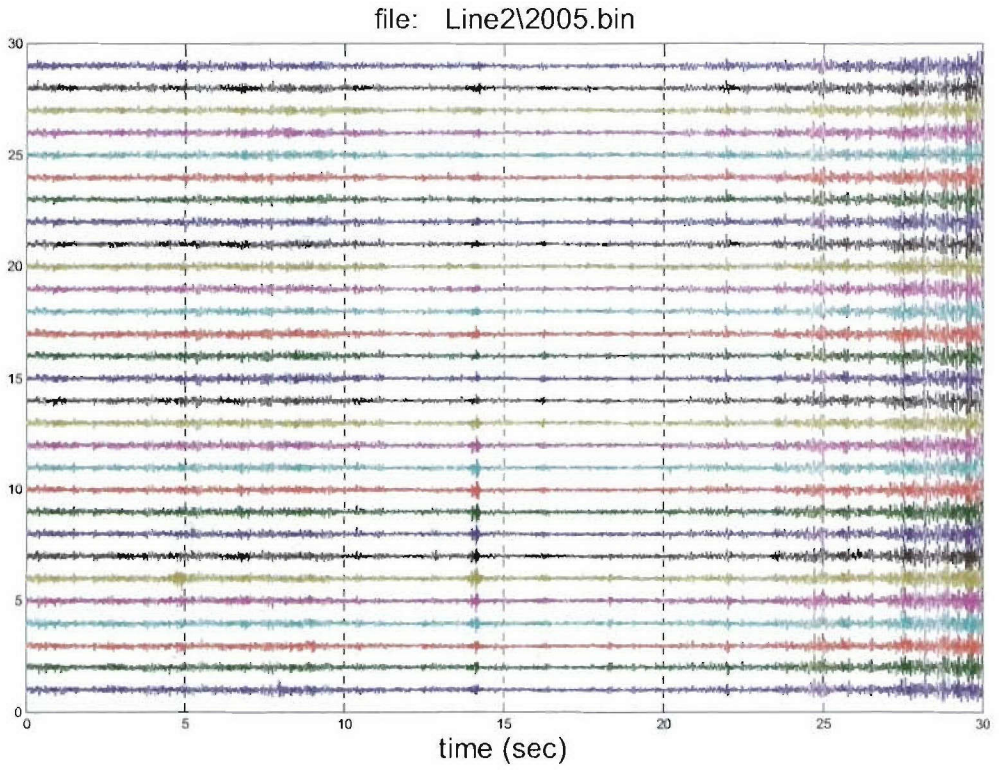

Figure 11. Traces of the raw data recorded by 29 geophones over 30 seconds. Notice the onset of activity toward the end of this record.

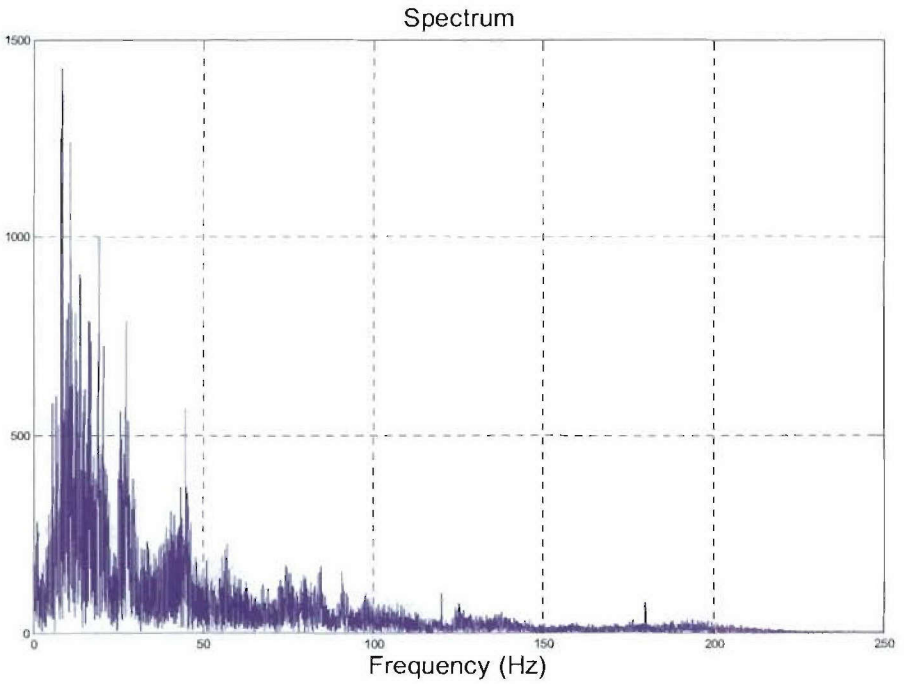

Figure 12. Spectrum of a single trace.

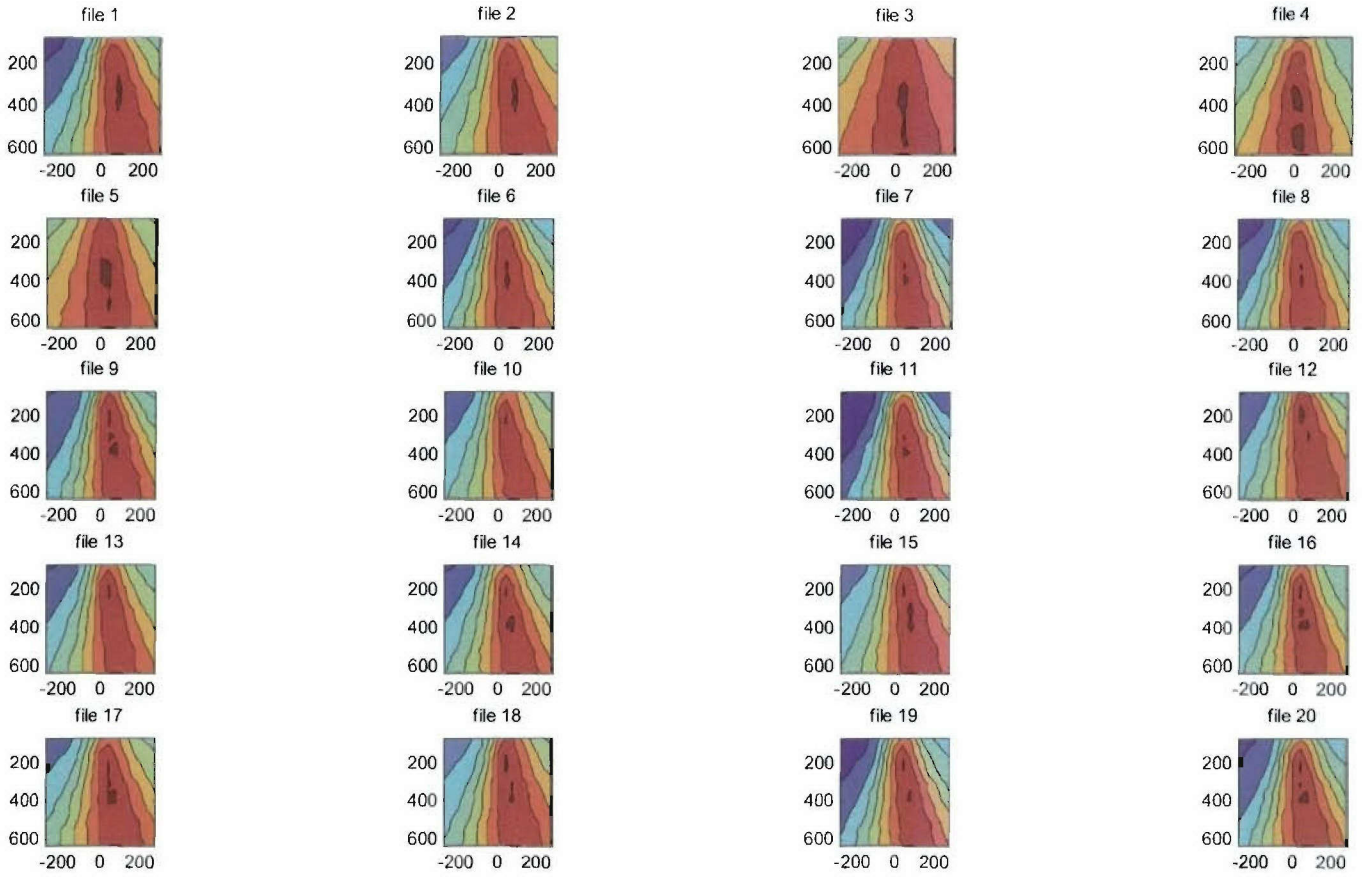

Figure 13a. Each image shown was derived from a separate 30 second data record from the Line 1 data set. Depth is downward. The peaks of the images are consistent with a localized source at a depth of 350 ft. The variability in the images is a result of the mining activity being intermittent.

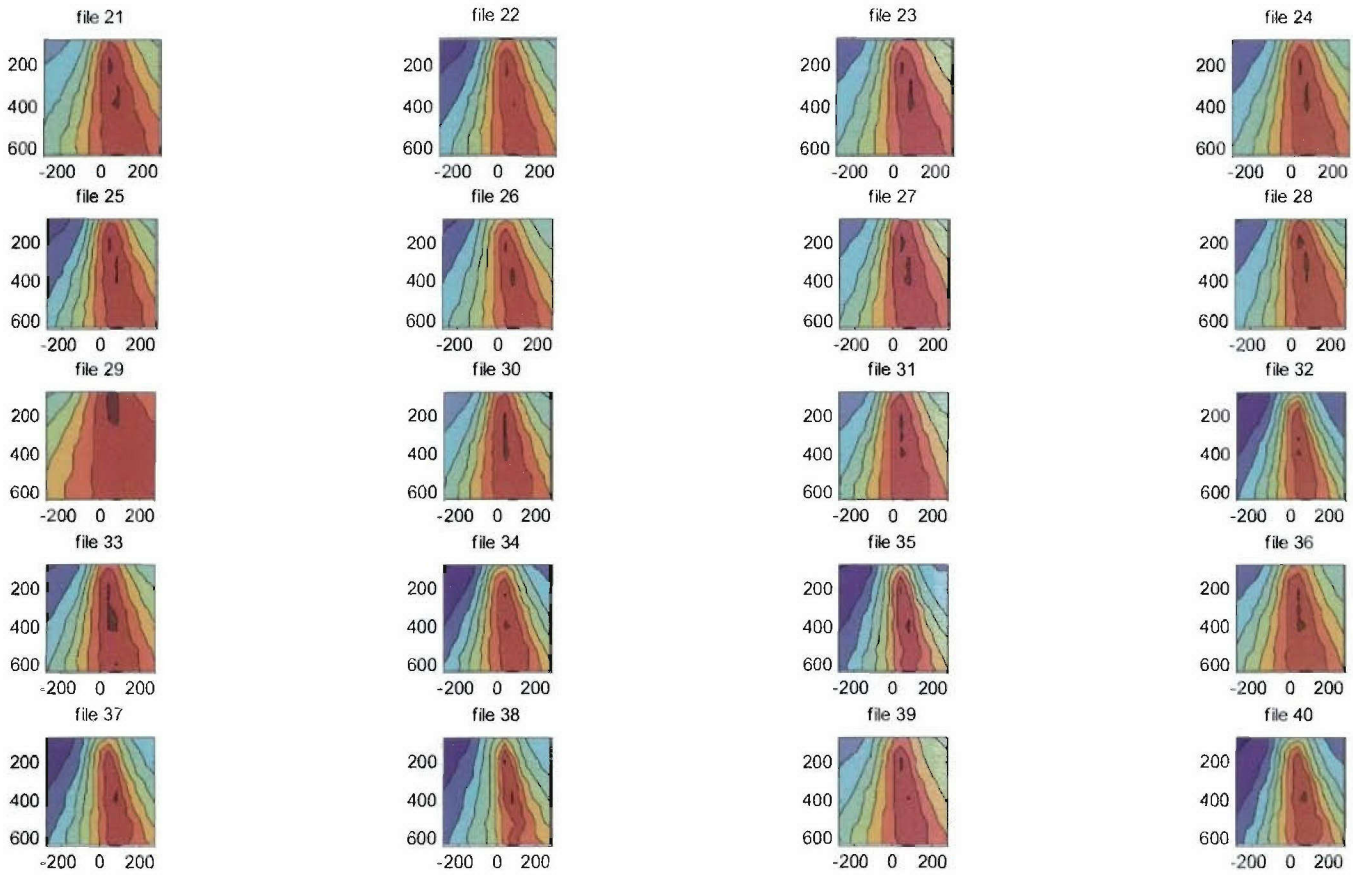

Figure 13b. 20 more images derived from the Line 1 data set.

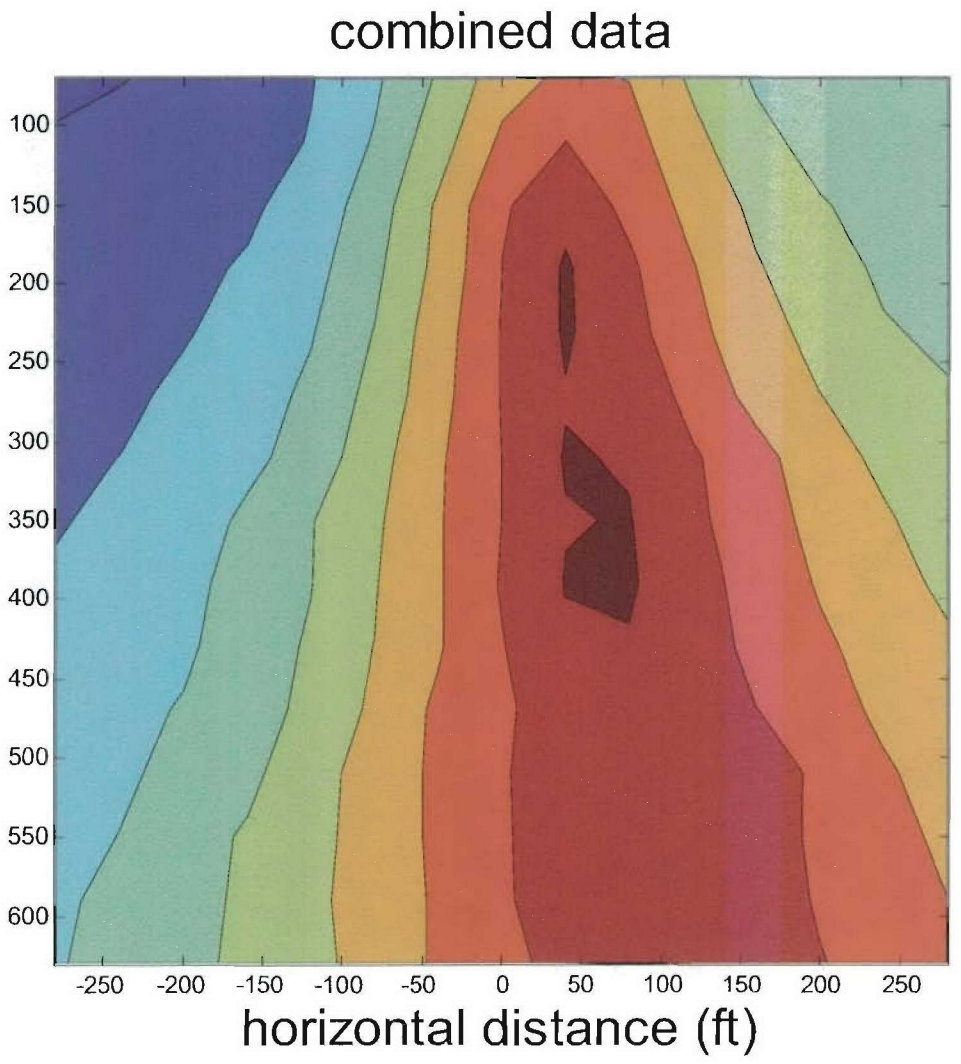

Figure 13c. The image obtained by combining all 40 data sets from the Line 1 array orientation. The source was at a depth of 350 feet.

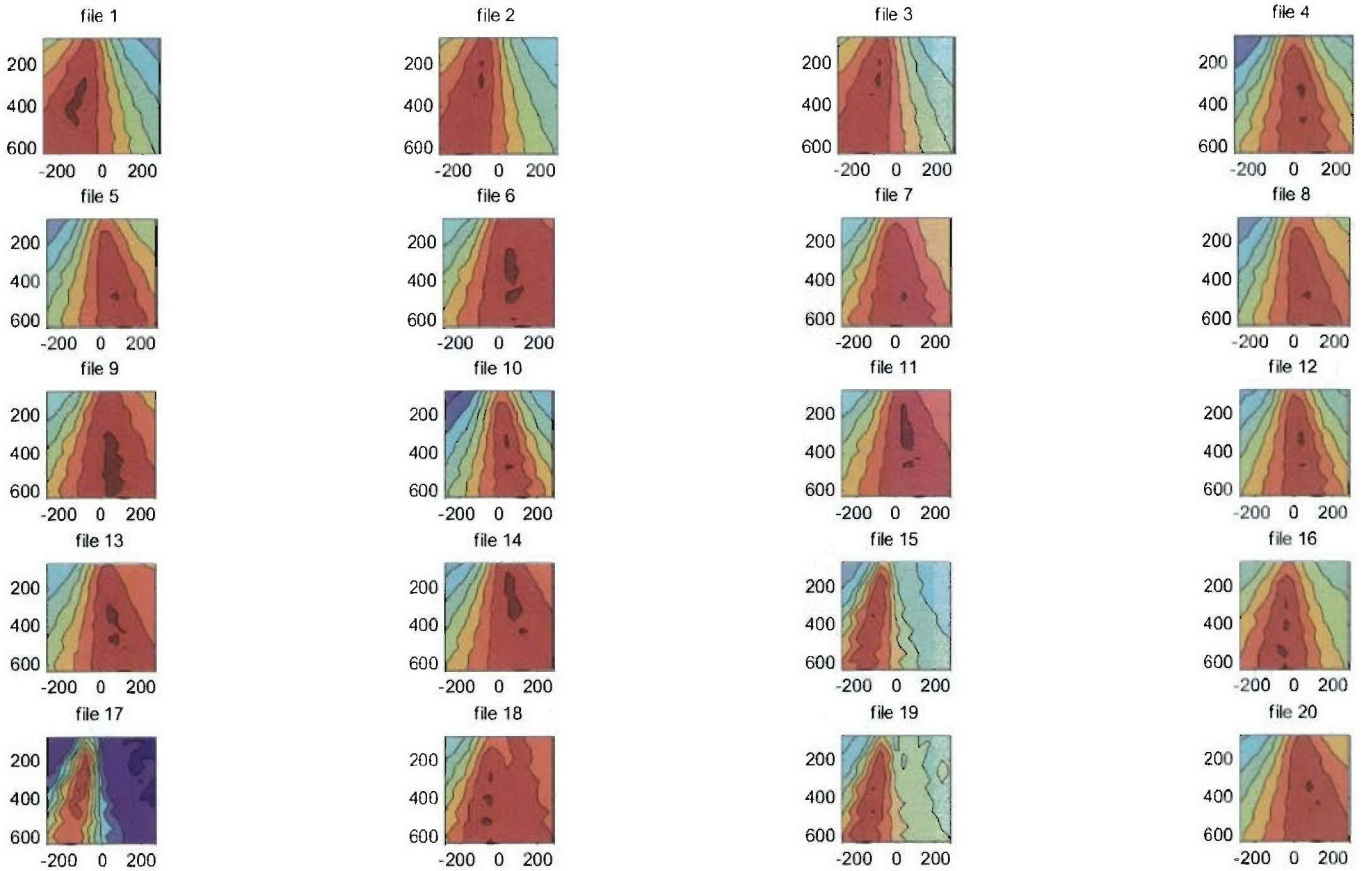

Figure 14a. Each image shown was derived from a separate 30 second data record from the Line 2 data set.

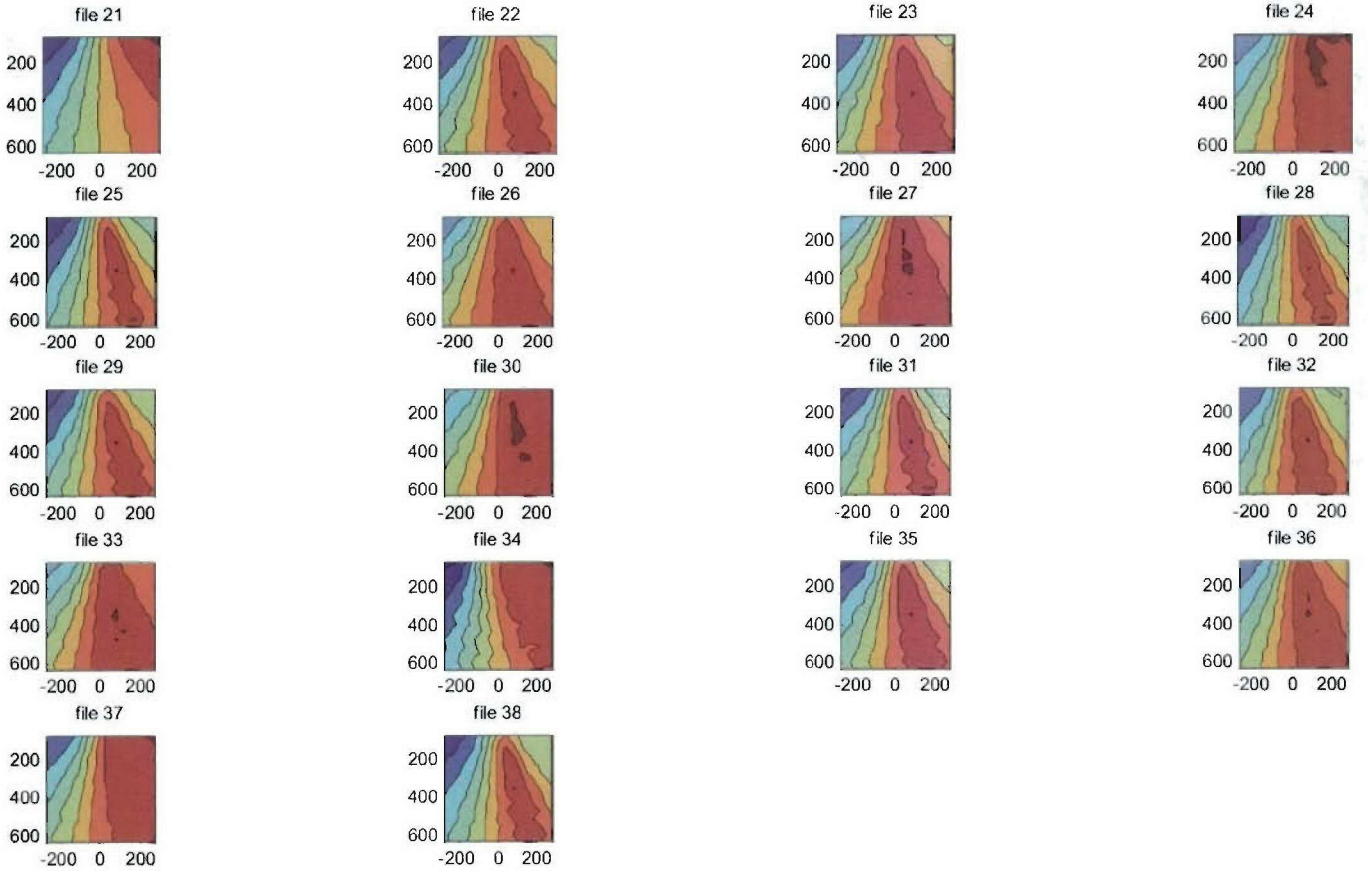

Figure 14b. 18 more images derived from the Line 2 data set.

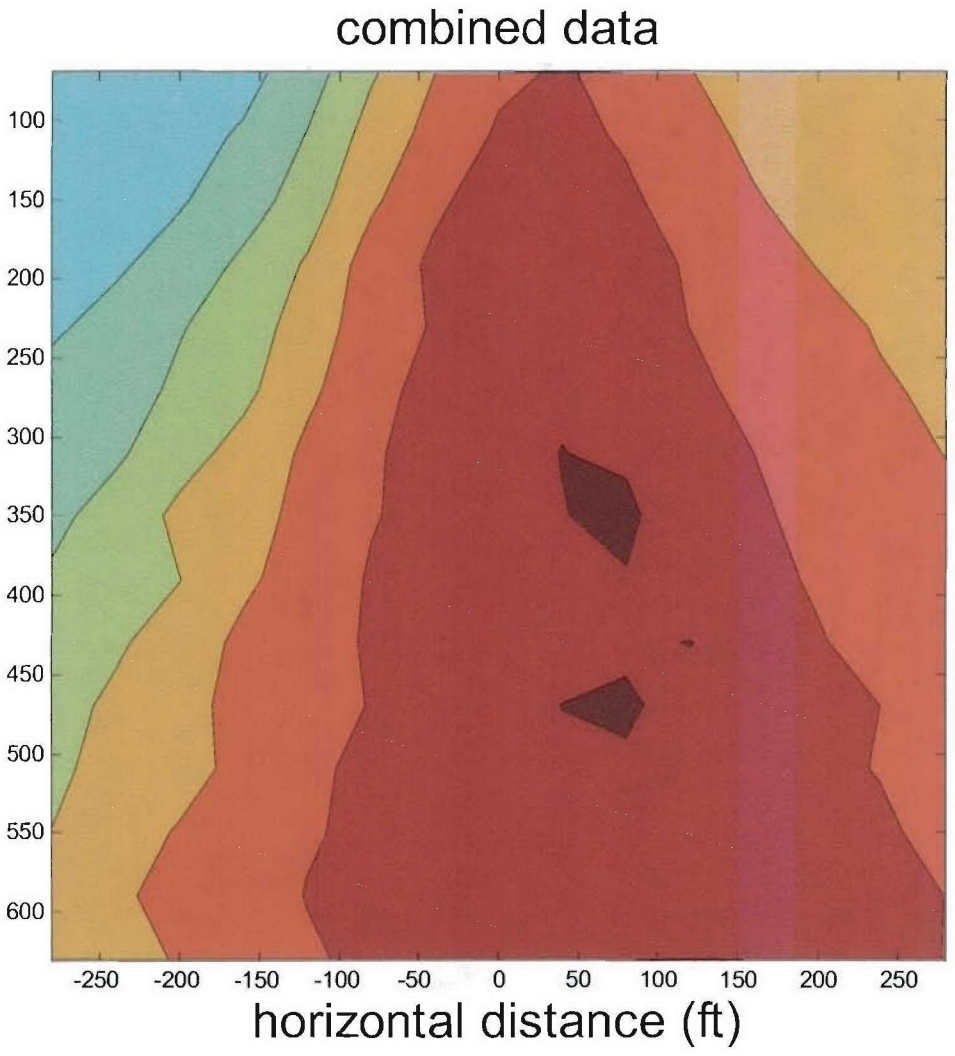

Figure 14c. The image obtained by combining all 38 data sets from the Line 2 array orientation.

5. Recommendations and Conclusions

The coalmine study demonstrates that passive imaging is feasible under realistic conditions, but improvements are certainly possible. For example, some noticeable phase rotation of the seismic traces across the array is evident when the traces are plotted (e.g., as in Figure 11 but at higher magnification). The phase rotation is probably due in part to dispersion of the seismic waves as a function of path length (greater path lengths imply greater dispersion). Phase rotation will degrade the resolution of the image. Simulations show that images derived from idealized data in the absence of phase rotation are of higher quality. No phase rotation implies that the signals recorded at different geophones are merely delayed versions of one another, where the delay is proportional to path length differences from the source to the receivers. Phase rotation due to dispersion can be corrected to some extend by inverse filtering, but was not attempted here. The reason for this is that rotation due to pure dispersion due only to path length differences was not clearly evident in the raw data, since systematic phase distortion as a function of path length was not seen across the array. This seems to imply that the phase distortion is probably due primarily to velocity inhomogeneities along the different propagation paths. Partial compensation for this might be achieved by incorporating a layered-earth model into the imaging algorithms, although this would require some a priori knowledge of the local stratigraphy.

Another improvement that could be made in future measurements would be to reduce the sampling interval to well below the 2 ms used here, since the difference in arrival time between adjacent phones was typically smaller than 2 ms (but sufficient to resolve delay differences between non-adjacent phones).

Since the arrays were linear, only 2-D images were obtained with no spatial resolution perpendicular to the array. Fully 3-D resolution would require a 2-D surface array. The optimum way to distribute a limited number of geophones in 2-D to achieve the best resolution would also require further study.

Another area that could be investigated to improve image quality and resolution is the use of adaptive imaging techniques, similar in concept to adaptive techniques used in astronomy to compensate for random phase errors arising from propagation through an inhomogeneous atmosphere [11-12]. This approach works well when one can identify a single isolated source whose image can be sharpened through an adaptive process involving the application of phase delays to the signals recorded over an aperture (in our case, the sensor array). These phase delays are selected to maximize some measure of image sharpness. Any sources that are nearby the "reference" source will also undergo sharpening as long as the propagation paths from nearby sources are similarly affected by local inhomogeneities in the propagating medium. This region for which sharpening occurs is known as an isoplanatic patch in optics. As far as we are aware, adaptive techniques have not been applied to passive or active seismic imaging. Certainly, the conditions are not as favorable as in astronomy (in which a single bright star typically serves as the isolated reference source), but if a dominant and isolated seismic source can

[11] R. A. Muller and A. Buffington, Real-time correction of atmospherically degraded telescope images through image sharpening, J. Opt. Soc. Am., vol. 64, pp. 1200-1210 (1974).

[12] S. J. Norton, Adaptive imaging in aberrating media: A broadband algorithm, Ultrasonic Imaging, vol. 14, pp. 300-321 (1992).

Appendix: Passive Imaging Algorithms

A. Time-Domain Migration Algorithm

Letting $\bar{u}(\mathbf{r}_n, t)$ denote the signal recorded by the n-th geophone, the imaging algorithm is given by the formula

$$\hat{\mathcal{I}}(\mathbf{r}) = \left\langle \left| \sum_{n=1}^{N} \bar{u}_n(\mathbf{r}) \right|^2 \right\rangle_{t_0} - \left\langle \sum_{n=1}^{N} |\bar{u}_n(\mathbf{r})|^2 \right\rangle_{t_0},$$

where

$$\bar{u}_n(\mathbf{r}) \equiv |\mathbf{r} - \mathbf{r}_n| \, \bar{u}(\mathbf{r}_n, |\mathbf{r} - \mathbf{r}_n|/c + t_0),$$

is the backprojected signal and the angle brackets denote a time average with respect to t_0.

B. Cross-Correlation Algorithm

Define the cross-correlation between the signals recorded by the m-th and n-th geophone as

$$\begin{aligned} \Gamma_{\bar{u}\bar{u}}(\mathbf{r}_n, \mathbf{r}_m; t, t') &= \langle \bar{u}(\mathbf{r}_n, t) \bar{u}(\mathbf{r}_m, t') \rangle_{t_0} \\ &\equiv \lim_{T \to \infty} \frac{1}{T} \int_0^T \bar{u}(\mathbf{r}_n, t + t_0) \bar{u}(\mathbf{r}_m, t' + t_0)^* \, dt_0. \end{aligned}$$

Then the cross-correlation image reconstruction algorithm is given by

$$\hat{\mathcal{I}}(\mathbf{r}) = \sum_{\substack{n=1 \\ n \neq m}}^{N} \sum_{m=1}^{N} |\mathbf{r} - \mathbf{r}_n| |\mathbf{r} - \mathbf{r}_m| \, \Gamma_{\bar{u}\bar{u}}(\mathbf{r}_n, \mathbf{r}_m; |\mathbf{r} - \mathbf{r}_n|/c, |\mathbf{r} - \mathbf{r}_m|/c).$$